

Cryogenic microwave source based on nanoscale tunnel junctions

Shumpei Masuda,^{*,†} Kuan Y. Tan,[†] Matti Partanen,[†] Russell E. Lake,[†] Joonas Govenius,[†] Matti Silveri,^{†,¶} Hermann Grabert,[‡] and Mikko Möttönen^{*,†}

QCD Labs, COMP Centre of Excellence, Department of Applied Physics, Aalto University, PO Box 13500, FI-00076 Aalto, Finland, and Department of Physics, University of Freiburg, Germany

E-mail: shumpei.masuda@aalto.fi; mikko.mottonen@aalto.fi

Abstract

We experimentally realize an incoherent microwave source driven by voltage-controlled quantum tunneling of electrons through nanoscale normal-metal–insulator–superconductor junctions coupled to a resonator. We observe the direct conversion of the electronic energy into microwave photons by measuring the power spectrum of the microwave radiation emitted from the resonator. The demonstrated total output power exceeds that of 2.5-K thermal radiation although the photon and electron reservoirs are at subkelvin temperatures. Measurements of the output power quantitatively agree with a theoretical model in a wide range of the bias voltages providing information on the electrically-controlled photon creation. The developed photon source is fully compatible with low-temperature electronics and offers convenient in-situ electrical control of the photon emission rate with a predetermined frequency, without relying on intrinsic voltage fluctuations of heated normal-metal components nor suffering from unwanted dissipation in room temperature cables. In addition to its potential applications in microwave

^{*}To whom correspondence should be addressed

[†]QCD Labs, COMP Centre of Excellence, Department of Applied Physics, Aalto University, PO Box 13500, FI-00076 Aalto, Finland

[‡]Department of Physics, University of Freiburg, Germany

[¶]Research Unit of Theoretical Physics, University of Oulu, FI-90014 Oulu, Finland

photonics, our results provide complementary verification of the working principles of the recently discovered quantum-circuit refrigerator.

Introduction

Superconducting circuits provide a promising platform for quantum technological applications,¹ such as quantum information processing,^{2–8} sensing,^{9–11} and refrigeration of electric components.^{12–15} In particular, microwave photons constitute a fundamental and controllable medium¹⁶ for energy and information transport between quantum electric components. For example, quantum-limited heat conduction between nanoelectronic components mediated by microwave photons has been measured,^{13,17} even through coplanar waveguides (CPW) across macroscopic distances.¹⁸

In this context, an on-chip tunable photon source with high dynamic range is desirable since it can provide reference photons with a given frequency for calibration of cryogenic devices such as microwave photon detectors.¹⁰ Importantly, the photons created on a chip minimize unwanted and difficult-to-calibrate losses which typically occur in microwave cables and connectors. Thus, on-demand creation of microwave photons^{19,20} and improvement of the dynamic range of the sources are fundamental to electric quantum circuits.

It is well known that tunneling of electrons across a nanoscale barrier can lead to energy exchange with the coupled electromagnetic environment such as a resonator.^{14,15,21–25} Consequently, several schemes of resonator state control based on the quantum tunneling of electrons have been introduced using, for example, Josephson junctions,^{26,27} superconducting qubits,^{28–31} and quantum dots.^{32–35} Even refrigeration of a superconducting microwave resonator mode has been demonstrated using controlled tunneling of single electrons across normal-metal–insulator–superconductor (NIS) tunnel junctions.¹⁴ Our photon source is based on similar tunneling of electrons across NIS junctions. It does not require any external magnetic fields to operate and can potentially offer a wide dynamic range and robust control of the output power, in contrast to, for

example, the one based on tunneling of Cooper pairs across a Josephson junction,²⁷ the power of which is determined by a sharp resonance condition in its bias voltage. To the best of our knowledge, no microwave photon source based on metallic NIS tunnel junctions has been demonstrated to date.

In this Letter, we report the fabrication and operation of a microwave source driven by single-electron tunneling through NIS junctions. The experimental setup is extended from that of the first quantum-circuit refrigerator,¹⁴ such that we can measure the power spectrum of the microwave radiation generated in a CPW resonator. The device is fully compatible with low-temperature electronics and offers orders of magnitude electrical tunability of the output power with the frequency corresponding to the lowest mode of the CPW resonator. Our results demonstrate that the effective mode temperature of the resonator can be driven beyond 2.5 K, far above the temperatures of the phonon and electron reservoirs of the system. Thus our source has potential in delivering relatively high powers without the excess heating of other nearby components.

Results

Samples and the measurement setup

The experimental sample shown in Figure 1a–c consists of NIS tunnel junctions capacitively coupled to a half-wave-length superconducting CPW resonator. Figure 1d depicts the layout of the sample and the measurement setup. Microwave photons, which are generated in the resonator at 10-mK phonon temperature, decay to the transmission line which is capacitively coupled to the resonator, and are characterized using a room temperature spectrum analyzer. To estimate the output power generated by controlled electron tunneling without off-sets, we subtract the output power corresponding to zero bias voltage across the superconductor–insulator–normal-metal–insulator–superconductor (SINIS) junction from the output power at finite bias voltages. As depicted in Figure 1b, a pair of NIS junctions is used to create the photons, while another pair is used as a thermometer to measure the electron temperature of the normal-metal island³⁶ (see Supporting

Information).

To enhance the interaction between the tunneling electrons and the resonator, we use a large coupling capacitance between the normal-metal island and the resonator, C_3 , in comparison to the tunnel junction capacitance, C_J . A small enough coupling capacitance between the resonator and the transmission line is employed to maintain a well-defined resonance described by the loaded resonator quality factor $Q \approx 60$. The length of the resonator is chosen to obtain the desired frequency of the output radiation. In this letter, we examine two samples with resonator lengths of $L_{\text{res}} = 13.14$ mm (Sample A) and $L_{\text{res}} = 6.89$ mm (Sample B) which correspond to the fundamental resonance frequencies of 4.55 GHz and 8.32 GHz, respectively.

Principle of photon generation

Photon-assisted electron tunneling is the key phenomenon leading to the photon creation in our experiments. When an electron tunnels across an NIS junction, it can absorb energy from or emit energy to the resonator, that is, annihilate or create photons in the resonator.²⁵ Figure 1e illustrates single-electron tunneling events across the NIS junctions and the associated photon creation. When the energy provided by the bias voltage to the electron tunneling across the junction, $eV_B/2$, is larger than the superconductor gap parameter, Δ , the photon creation rate increases faster as a function of the bias voltage than the annihilation rate. Thus, the effective temperature related to the creation and annihilation of photons increases. The elastic tunneling does not directly affect the resonator modes but dominates the electric current across the junctions for $eV_B/(2\Delta) \gtrsim 1$.

Experiments on Sample A

Figure 2a,b shows the output power spectrum of our microwave source as a function of the bias voltage for Sample A. We observe a peak in the output power density around 4.55 GHz matching the frequency of the fundamental resonator mode estimated using the experimental parameters given in Table 1. The output power density increases with the bias voltage for $eV_B/(2\Delta) > 1$ whereas it is almost vanishing for $|eV_B/(2\Delta)| < 1$. This onset of output radiation matching the

energy gap in the superconductor density of states provides clear evidence that single-electron tunneling is responsible for the observed photon emission. The bias-voltage dependence of the frequency-integrated output power density, i.e., the net output power is shown in Figure 2c. The onset of positive net power is clearly visible at $eV_B/(2\Delta) = 1$.

Theoretically, the net output power is related to the average photon numbers of the resonator, \bar{n}_{res} , and the transmission line, \bar{n}_{TL} , at the fundamental angular frequency, ω_0 , by (see Supporting Information)

$$P_{\text{RT}} = \frac{2C_4^2 \hbar \omega_0^3 Z_0}{L_{\text{res}} c_{\text{res}}} (\bar{n}_{\text{res}} - \bar{n}_{\text{TL}}), \quad (1)$$

where Z_0 is the characteristic impedance of the transmission line and c_{res} is the capacitance per unit length of the resonator. In our experiments, the resonator mode is in a thermal state, and hence we may describe its average photon numbers using the Bose distribution function as

$$\bar{n}_{\text{res}} = \frac{1}{\exp[\hbar \omega_0 / (k_B T_{\text{res}})] - 1}. \quad (2)$$

With a given \bar{n}_{TL} , the above equations provide an analytic way of extracting the resonator temperature, T_{res} , and average photon number directly from the output power.

Although we measure only the difference in the output powers at finite and zero bias voltages, we assume for simplicity that the net output power at zero bias voltage vanishes, i.e., here the resonator is thermalized with the transmission line. This assumption does not lead to changes in the estimated T_{res} , but renders \bar{n}_{TL} to describe the cumulative voltage-bias-independent heating effect of the resonator owing to the transmission line and any additional environments (see Supporting Information). Consequently, we refer below to T_{TL} as the apparent transmission line temperature. Note that the estimated resonator temperature becomes insensitive to changes in T_{TL} at high bias voltages where $\bar{n}_{\text{res}} \gg \bar{n}_{\text{TL}}$.

Figure 2d shows the resonator temperature and average photon number corresponding to the measured output power in Figure 2c as functions of the bias voltage. These results indicate that

the mode temperature and the average photon number can be efficiently controlled using the bias voltage. For $eV_B > 10\Delta$, we have $T_{\text{res}} > 2.5$ K. Such a high mode temperature is not conveniently achieved by coupling the resonator to a hot resistor due to the transition of the superconducting aluminum, employed as the lead material, to the normal state.

As mentioned above, the electron temperature at the normal-metal island of the NIS junctions is measured using a pair of NIS junctions (see Supporting Information). Importantly, the electron temperature shown in Figure S4b is much lower than that of the resonator mode for almost any bias voltage in Figure 2c,d. This observation verifies that the microwave radiation observed by the spectrum analyzer directly arises from photon-assisted electron tunneling rather than from heating of the normal-metal island.

Although negative net output power is challenging to differentiate in the measured power spectra, we observe in Figure 2c a shallow but statistically significant dip in the experimental output power around $eV_B/(2\Delta) = 1$. The dip corresponds to the refrigeration of the fundamental mode owing to photon-assisted tunneling, and hence provides complementary evidence of this phenomenon first observed in Ref. 14. In contrast to our measurements of the output radiation, Ref. 14 employs a probe resistor to study the resonator temperature.

Thermal model

To describe in detail the energy transfer from the tunneling electrons to the transmission line, mediated by microwave photons in the fundamental mode of the resonator, we develop a thermal model shown in Figure 3. Here, we consider thermal states for the electric components assuming that the temperatures of the resonator mode, T_{res} , and of the electrons in the normal-metal island, T_N , are well defined in the parameter range studied. We have verified the validity of this assumption with a model that accounts for transitions between individual resonator states but do not present the model here since it is unnecessarily complicated. Because of the relatively weak coupling between the resonator and the transmission line, we assume that a tunneling electron does not directly induce photon-assisted transitions in the transmission line. Instead, the influence of the tunneling

events is indirectly taken into account through the change in the temperature of the resonator mode.

In the thermal model, the power from the tunneling electrons to the resonator, P_{JR} , is calculated using the $P(E)$ theory,²⁵ as detailed in Supporting Information together with the above-discussed power flow from the resonator to the transmission line, P_{RT} . Both of these powers are functions of the temperature of the resonator mode. The output power into the transmission line is calculated by finding the mode temperature, at which these powers balance, $P_{\text{JR}} = P_{\text{RT}}$. The apparent temperature of the transmission line, corresponding to the photons moving towards the resonator and possible additional heating channels, is assumed to be independent of the applied bias voltage. This is justified for the photons by the employed circulator shown in Figure 1d. The experimentally measured electron temperature of the normal-metal island is used in the simulation.

The theoretical results, employing the parameters given in Table 1, show good agreement with the experiments in a wide range of output powers (see Figure 2c). In the model, the dip in the output power around $eV_{\text{B}}/(2\Delta) = 1$ is fully arising from photon absorption induced by electron tunneling. Furthermore, the modelled average number of photons, \bar{n}_{res} , and the temperature of the fundamental mode, T_{res} , are shown in Figure 2d as functions of the bias voltage.

Experiments on Sample B

Experimental results similar to those discussed above are shown in Figure 4 for Sample B. Figure 4a shows the output power density as a function of the frequency and the bias voltage. A peak appears around 8.3 GHz for $eV_{\text{B}}/(2\Delta) > 1$ and becomes taller with increasing bias voltage. Figure 4b exhibits the traces of the output power density, which are integrated for Figure 4c to obtain the net output power as a function of the bias voltage. The qualitative behavior of the output power matches that of Sample A: the output power begins to increase with bias voltage around $eV_{\text{B}}/(2\Delta) = 1$, where we observe a shallow dip corresponding to cooling of the resonator. However, the magnitude of the output power is greater and the mode temperature shown in Figure 4d is lower compared with Figure 2. This is because the coupling of the resonator to the transmission line is proportional to the third power of the resonance frequency [see Eq. (1)] which is almost

twice as large here in comparison to Sample A.

Discussion

In conclusion, we have measured the spectrum of microwave radiation generated by photon-assisted electron tunneling through NIS junctions. The implemented microwave source realizes direct conversion of the electrostatic energy provided by the dc voltage source to microwave photons. Importantly, it does not rely on the thermal voltage fluctuation spectrum of a resistor, and hence may provide higher effective temperatures, faster tunability, and less excess heating than usual thermal methods. Namely, our results demonstrate the control of the output power up to the regime where the effective mode temperature of the resonator is higher than the critical temperature of the widely used aluminum. The device is compatible with low-temperature electronics and offers in-situ electrical tunability of the output power with the frequency predetermined by the associated resonator. Our measurements of the output power are in good agreement with the corresponding theoretical model, heavily suggesting that our interpretation that photon-assisted tunneling is mainly responsible for the output power is correct. This interpretation is verified by the observation of much higher output powers than what is expected for resonator temperatures matching the normal-metal electron temperature.

Methods

Sample fabrication

The experimental sample shown in Figure 1a–c is fabricated on a high-purity 500- μm -thick silicon wafer. The silicon substrate is passivated with a 300-nm-thick thermally grown silicon dioxide. The half-wave-length superconducting CPW resonator is defined with photolithography and reactive ion etching of a 200-nm-thick sputtered Nb layer. Subsequently, a 50-nm-thick layer of Al_2O_3 is introduced on the whole wafer using atomic layer deposition (ALD) process at 200 °C. This ALD

oxide serves as the dielectric material of the parallel plate capacitors C_{1-4} shown in Figure 1d. The NIS junctions and a transmission line connected to the resonator are subsequently defined using electron beam lithography, followed by a standard two-angle evaporation with in-situ oxidation to form the tunnel barriers. The final NIS nano-structure consists of a 20-nm-thick normal metal (Cu) on top of a 20-nm-thick superconductor (Al), separated by a thin aluminum-oxide tunnel barrier.

Supporting Information

The Supporting Information is available free of charge. Parameters, Apparent transmission line temperature, Energy transfer between tunneling electron and resonator, Energy transfer between resonator and transmission line, Thermometer.

Corresponding Authors

*E-mail: shumpei.masuda@aalto.fi *E-mail: mikko.mottonen@aalto.fi

Author Contributions

Authors S.M. and K.Y.T fabricated the samples and conducted the experiments. S.M. also developed the model and analysed the data. M.P. contributed to the sample fabrication, measurements, and data analysis. R.L. and J.G. contributed to the measurements. M.S and H.G. contributed to the theoretical analysis. M.M. provided the initial ideas and suggestions for the experiment, and supervised the work in all respects. All authors commented on the manuscript written by S.M. and M.M.

Competing Financial Interest

The authors declare no competing financial interest.

Acknowledgement

We acknowledge the provision of facilities and technical support by Aalto University at OtaNano - Micronova Nanofabrication Centre. We have received funding from the European Research Council under Starting Independent Researcher Grant No. 278117 (SINGLEOUT) and under Consolidator Grant No. 681311 (QUESS), the Academy of Finland through its Centres of Excellence Program (project nos 251748 and 284621) and grants (Nos. 265675, 286215, 276528, 305237, and 305306), the Emil Aaltonen Foundation, the Jenny and Antti Wihuri Foundation, the Alfred Kordelin Foundation, and the Finnish Cultural Foundation. We thank Leif Grönberg for assistance in sample fabrication.

References

- (1) Wolf, E. L. *Quantum Nanoelectronics: An Introduction to Electronic Nanotechnology and Quantum Computing* (Wiley-VCH, Weinheim, 2009).
- (2) Blais, A., Huang, R. -S., Wallraff, A., Girvin, S. M. & Schoelkopf, R. J. Cavity quantum electrodynamics for superconducting electrical circuits: An architecture for quantum computation. *Phys. Rev. A* **69**, 062320 (2004).
- (3) Wallraff, A., Schuster, D. I., Blais, A., Frunzio, L., Huang, R.-S., Majer, J., Kumar, S., Girvin, S. M. & Schoelkopf, R. J. Strong coupling of a single photon to a superconducting qubit using circuit quantum electrodynamics. *Nature* **431**, 162–167 (2004).
- (4) Majer, J., Chow, J. M., Gambetta, J. M., Koch, J., Johnson, B. R., Schreier, J. A., Frunzio, L., Schuster, D. I., Houck, A. A., Wallraff, A., Blais, A., Devoret, M. H., Girvin, S. M. & Schoelkopf, R. J. Coupling superconducting qubits via a cavity bus. *Nature* **449**, 443–447 (2007).
- (5) Sillanpää, M. A., Park, J. I. & Simmonds, R. W. Coherent quantum state storage and transfer between two phase qubits via a resonant cavity. *Nature* **449**, 438–442 (2007).

- (6) Devoret, M. H. & Schoelkopf, R. J. Superconducting circuits for quantum information: an outlook. *Science* **339**, 1169–1174 (2013).
- (7) Kelly, J. et al. State preservation by repetitive error detection in a superconducting quantum circuit. *Nature* **519**, 66–69 (2015).
- (8) Ofek, N. et al. Extending the lifetime of a quantum bit with error correction in superconducting circuits. *Nature* **536**, 441–445 (2016).
- (9) Inomata, K., Lin, Z. R., Koshino, K., Oliver, W. D., Tsai, J. S., Yamamoto, T. & Nakamura, Y. Single microwave-photon detector using an artificial Λ -type three-level system. *Nat. Commun.* **7**, 12303 (2016).
- (10) Govenius, J., Lake, R. E., Tan, K. Y. & Möttönen, M. Detection of Zeptojoule microwave pulses using electrothermal feedback in proximity-induced Josephson junctions. *Phys. Rev. Lett.* **117**, 030802 (2016).
- (11) Saira, O.-P., Zgirski, M., Viisanen, K. L., Golubev, D. S. & Pekola, J. P. Dispersive thermometry with a Josephson junction coupled to a resonator. *Phys. Rev. Applied* **6**, 024005 (2016).
- (12) Clark, A. M., Miller, N. A., Williams, S., Ruggiero, S. T., Hilton, G. C., Vale, L. R., Beall, K. D., Irwin, K. D. & Ullom, J. N. Cooling of bulk material by electron-tunneling refrigerators. *Appl. Phys. Lett.* **86**, 173508–173510 (2005).
- (13) Timofeev, A. V., Helle, M., Meschke, M., Möttönen, M. & Pekola, J. P. Electronic refrigeration at the quantum limit. *Phys. Rev. Lett.* **102**, 200801 (2009).
- (14) Tan, K. Y., Partanen, M., Lake, R. E., Govenius, J., Masuda, S. & Möttönen, M. Quantum-circuit refrigerator. *arXiv:1606.04728* (2016).
- (15) Giazotto, F., Heikkilä, T. T., Luukanen, A., Savin, A. M. & Pekola, J. P. Opportunities for

- mesoscopics in thermometry and refrigeration: Physics and applications. *Rev. Mod. Phys.* **78**, 217–274 (2006).
- (16) Hofheinz, M., Wang, H., Ansmann, M., Bialczak, R. C., Lucero, E., Neeley, M., O’Connell, A. D., Sank, D., Wenner, J., Martinis, J. M. & Cleland, A. N. Synthesizing arbitrary quantum states in a superconducting resonator. *Nature* **459**, 546–549 (2009).
- (17) Meschke, M., Guichard, W. & Pekola, J. P. Single-mode heat conduction by photons. *Nature* **444**, 187–190 (2006).
- (18) Partanen, M., Tan, K. Y., Govenius, J., Lake, R. E., Mäkelä, K., Tanttu, T. & Möttönen, M. Quantum-limited heat conduction over macroscopic distances. *Nat. Phys.* **12**, 460–464 (2016).
- (19) Houck, A. A., Schuster, D. I., Gambetta, J. M., Schreier, J. A., Johnson, B. R., Chow, J. M., Frunzio, L., Majer, J., Devoret, M. H., Girvin, S. M. & Schoelkopf, R. J. Generating single microwave photons in a circuit. *Nature* **449**, 328–331 (2007).
- (20) Peng, Z. H., de Graaf, S. E., Tsai, J. S. & Astafiev, O. V. Tuneable on-demand single-photon source in the microwave range. *Nat. Commun.* **449**, 12588 (2016).
- (21) Pekola, J. P., Maisi, V. F., Kafanov, S., Chekurov, N., Kemppinen, A., Pashkin, Y. A., Saira, O. -P., Möttönen M. & Tsai, J. S. Environment-assisted tunneling as an origin of the Dynes density of states. *Phys. Rev. Lett.* **105**, 026803 (2010).
- (22) Devoret, M. H., Esteve, D., Grabert, H., Ingold, G.-L., Pothier, H. & Urbina, C. Effect of the electromagnetic environment on the Coulomb blockade in ultrasmall tunnel junctions. *Phys. Rev. Lett.* **64**, 1824 (1990).
- (23) Girvin, S. M., Glazman, L. I., Jonson, M., Penn, D. R. & Stiles, M. D. Quantum fluctuations and the single-junction Coulomb blockade. *Phys. Rev. Lett.* **64**, 3183 (1990).

- (24) Averin, B., Nazarov, Y. & Odintsov, A. Incoherent tunneling of the cooper pairs and magnetic flux quanta in ultrasmall Josephson junctions. *Physica B* **165/166**, 945–946 (1990).
- (25) Ingold, G. & Nazarov, Y. V. Charge tunneling rates in ultrasmall junctions. *NATO ASI Series B* **294**, 21–107 (1992).
- (26) Zakka-Bajjani, E., Dufouleur, J., Coulombel, N., Roche, P., Glatthli, D. C. & Portier, F. Experimental determination of the statistics of photons emitted by a tunnel junction. *Phys. Rev. Lett.* **104**, 206802 (2010).
- (27) Hofheinz, M., Portier, F., Baudouin, Q., Joyez, P., Vion, D., Bertet, P., Roche, P. & Esteve, D. Bright side of the coulomb blockade. *Phys. Rev. Lett.* **106**, 217005 (2011).
- (28) You, J. Q., Liu, Y. X., Sun, C. P. & Nori, F. Persistent single-photon production by tunable on-chip micromaser with a superconducting quantum circuit. *Phys. Rev. B* **75**, 104516 (2007).
- (29) Astafiev, O., Inomata, K., Niskanen, A. O., Yamamoto, T., Pashkin, Y. A., Nakamura, Y. & Tsai, J. S. Single artificial-atom lasing. *Nature* **449**, 588–590 (2007).
- (30) Hauss, J., Fedorov, A., Hutter, C., Shnirman, A. & Schön, G. Single-qubit lasing and cooling at the Rabi frequency. *Phys. Rev. Lett.* **100**, 037003 (2008).
- (31) Grajcar, M., van der Ploeg, S. H. W., Izmalkov, A., Ilichev, H. G. M. E., Fedorov, A., Shnirman, A. & Schön, G. Sisyphus cooling and amplification by a superconducting qubit. *Nat. Phys.* **4**, 612–616 (2008).
- (32) Bruhat, L. E., Viennot, J. J., Dartailh, M. C., Desjardins, M. M., Kontos, T. & Cottet, A. Cavity photons as a probe for charge relaxation resistance and photon emission in a quantum dot coupled to normal and superconducting continua. *Phys. Rev. X* **6**, 021014 (2016).
- (33) Stockklauser, A., Maisi, V. F., Basset, J., Cujia, K., Reichl, C., Wegscheider, W., Ihn, T., Wallraff, A. & Ensslin, K. Microwave emission from hybridized states in a semiconductor charge qubit. *Phys. Rev. Lett.* **115**, 046802 (2015).

- (34) Childress, L., Sørensen, A. S. & Lukin, M. D. Mesoscopic cavity quantum electrodynamics with quantum dots. *Phys. Rev. A* **69**, 042302 (2004).
- (35) Liu, Y.-Y., Petersson, K. D., Stehlik, J., Taylor, J. M. & Petta, J. R. Photon emission from a cavity-coupled double quantum dot. *Phys. Rev. Lett.* **113**, 036801 (2014).
- (36) Leivo, M. M. & Pekola, J. P. *Appl. Phys. Lett.* **68**, 1996–1998 (1996).
- (37) Gevorgian, S., Linnér, L. J. P. & Kollberg, E. L. CAD models for shielded multilayered CPW. *IEEE Trans. Microw. Theory Techn.* **43**, 772–779 (1995).
- (38) Göppl, M., Fragner, A., Baur, M., Bianchetti, R., Filipp, S., Fink, J. M., Leek, P. J., Puebla, G., Steffen, L. & Wallraff, A. Coplanar waveguide resonators for circuit quantum electrodynamics. *J. Appl. Phys.* **104**, 113904–113911 (2008).

Figures and tables

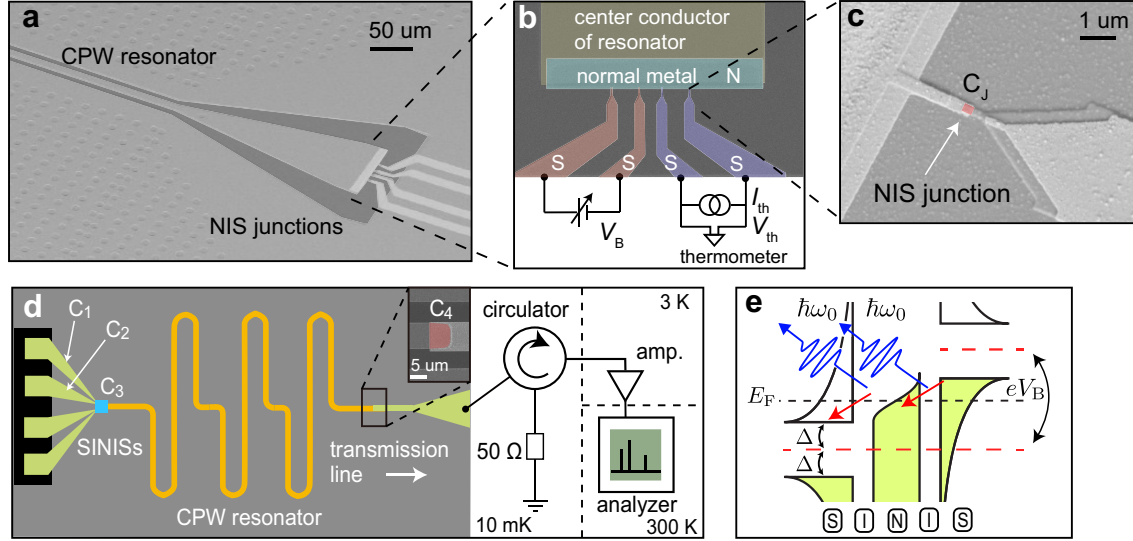


Figure 1: (a) Scanning-electron microscope (SEM) image of a fabricated device illustrating the CPW resonator and the NIS junctions operating together as the microwave source. (b) Colored SEM image of the NIS junctions. The junctions highlighted in red are used to excite the resonator using the bias voltage V_B . The junctions highlighted in blue are used as a thermometer to measure the electron temperature of the normal-metal island. (c) SEM image of an NIS junction highlighted in red. (d) Device design and measurement scheme. Here, C_{1-2} , C_3 , and C_4 denote the coupling capacitances between the bonding pads and the ground plane, between the normal-metal island of the NIS junctions and the center conductor of the resonator, and between the resonator and the transmission line (see inset), respectively, and C_J denotes the junction capacitance. The area indicated by the blue square corresponds to panel (a) although the axis of view is different. (e) Energy diagram for photon-assisted single-electron tunneling at bias voltage $eV_B/(2\Delta) > 1$, where Δ is the superconductor gap parameter and $\hbar\omega_0$ is the energy of an emitted photon. The black solid curves at the normal metal and the superconductors represent the Fermi–Dirac distribution function and the density of states in the superconductors, respectively. The colored areas represent the occupied states.

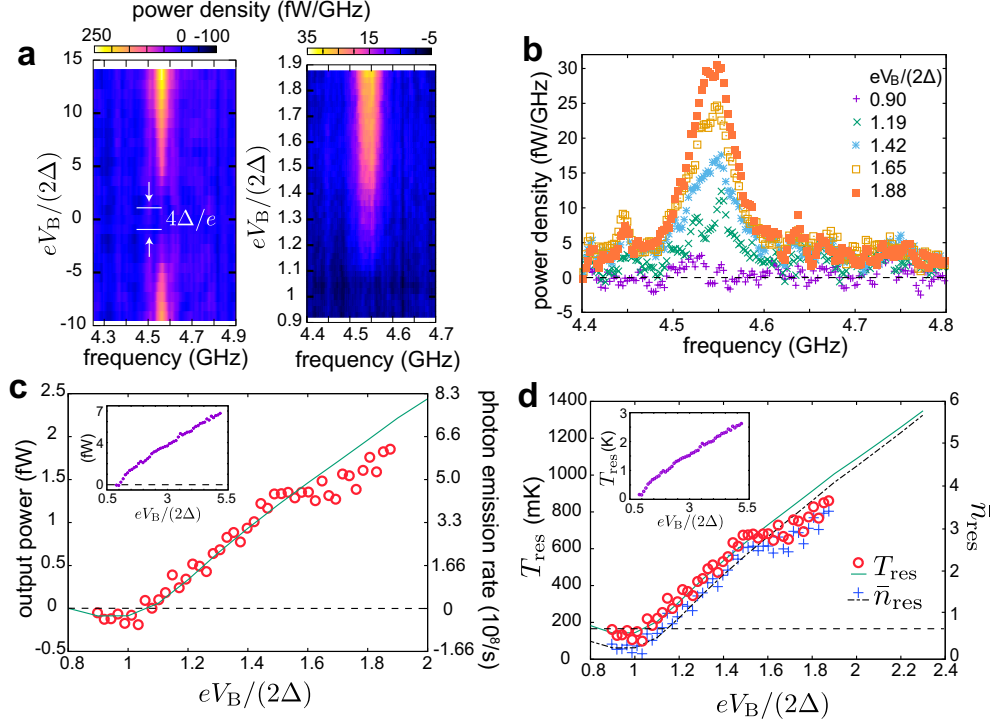


Figure 2: Experimental and numerical results for Sample A with the fundamental resonance frequency $f_0 = 4.55$ GHz. (a) Resonator output power densities measured as functions of frequency and bias voltage. Each frequency trace is measured by a spectrum analyzer as shown schematically in Figure 1d and averaged over 21000 repetitions. In addition, we employ a three-point moving average in frequency. The left panel shows the output power spectrum in a wider voltage range compared with the right panel. In contrast to Figure 1d, no circulator was used for the data in the left panel. (b) Output power densities as functions of frequency for the indicated bias voltages. The horizontal dashed line indicates the zero level corresponding to zero bias voltage. (c) Output power obtained by integrating data as in (b) from 4.4 GHz to 4.8 GHz as a function of the bias voltage. The green curve indicates the theoretical prediction of the thermal model illustrated in Figure 3. The inset shows the output power for an extended bias voltage range. The horizontal dashed lines indicate the zero level. (d) Average photon number (blue crosses) and temperature (red circles) of the fundamental mode as functions of the bias voltage obtained using the experimental results in (c) and Eqs. (1) and (2). The parameters are given in Table 1. Here, the dashed and solid curves represent \bar{n}_{res} and T_{res} obtained from the thermal model, respectively. We used a 38.5-dB cryogenic amplifier, 24-dB room temperature amplifier, and 6-dB room temperature attenuator. We assumed 15.9 dB of loss from the PCB and rf cables as opposed to 13.3 dB measured using a control sample. The horizontal dashed line indicates the apparent temperature of the transmission line as given in Table 1.

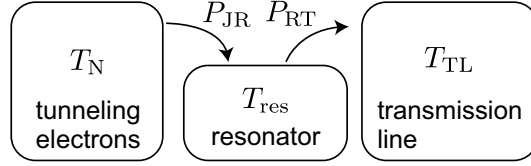


Figure 3: Thermal model of the device indicating the relevant temperatures and energy flows. The temperature of the fundamental resonator mode, T_{res} , becomes higher than the apparent temperature of the transmission line, T_{TL} , when the applied bias voltage strongly drives the photon creation. Here, T_N is the electron temperature at the normal-metal island of the NIS junctions. At steady state, the power P_{JR} from the tunneling electrons to the resonator and the power P_{RT} from the resonator to the transmission line balance, $P_{\text{JR}} = P_{\text{RT}}$. See Supporting Information for details.

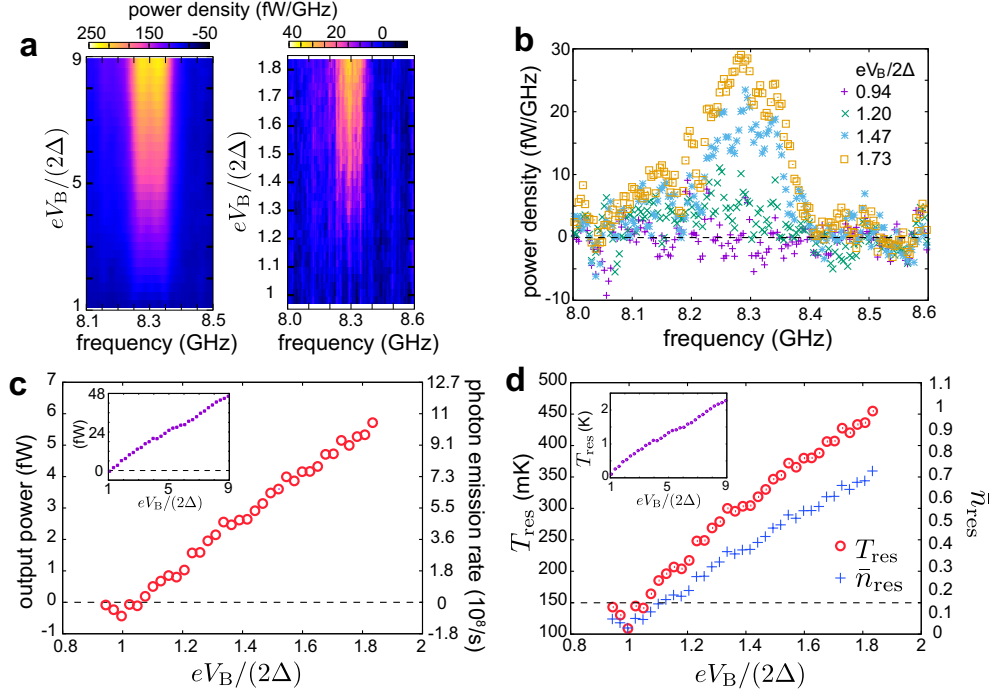


Figure 4: Experimental results for Sample B with the fundamental resonance frequency $f_0 = 8.3$ GHz. (a) Resonator output power densities measured as functions of frequency and bias voltage. Each frequency trace is measured by a spectrum analyzer as shown schematically in Figure 1d and averaged over 21000 repetitions. In addition, we employ a three-point moving average in frequency. The left panel shows the output power spectrum in a wider voltage range compared with the right panel. (b) Output power densities as functions of frequency for the indicated bias voltages. The horizontal dashed line indicates the zero level. (c) Output power obtained by integrating data as in (b) from 8.0 GHz to 8.6 GHz as a function of the bias voltage. The inset shows the output power for an extended bias voltage range. The horizontal dashed lines indicate the zero levels. (d) Average photon number (blue crosses) and temperature (red circles) of the fundamental mode as functions of the bias voltage obtained using the data in (c) and Eqs. (1) and (2). The parameters are given in Table 1. We used a 40-dB cryogenic amplifier, 24-dB room temperature amplifier, and 6-dB room temperature attenuator. We assumed 22 dB of loss from the PCB and rf cables as opposed to 19.5 dB measured using a control sample. The horizontal dashed line indicates the apparent temperature of the transmission line as given in Table 1. In contrast to Figure 2c,d, we do not show theoretical results here due to the lack of reliable temperature data for the normal-metal island.

Table 1: Parameters of the experimental samples: the length of the resonator L_{res} , superconductor gap parameter Δ , Dynes parameter γ_D , capacitance per unit length c_{res} , inductance per unit length l_{res} , fundamental resonance frequency f_0 , tunnel resistance R_T , junction capacitance C_J , capacitance $C_{3/4}$, characteristic impedance of the transmission line Z_0 , apparent temperature of transmission line T_{TL} , the employed attenuation of the PCB and rf cables α , the width of the center conductor w , and the separation between the center conductor and the ground plane of the CPW resonator s . Capacitance $C_{1/2}$ is more than 50 times larger than C_3 .

	SAMPLE A	SAMPLE B		SAMPLE A	SAMPLE B
L_{res}	13.14 mm	6.89 mm	C_3	0.84 pF	0.78 pF
Δ	220 μeV	191 μeV	C_4	0.072 pF	0.079 pF
γ_D	4×10^{-4}	4×10^{-4}	Z_0	53 Ω	52 Ω
c_{res}	159 pF/m	169 pF/m	T_{TL}	180 mK	150 mK
l_{res}	0.45 $\mu\text{H/m}$	0.45 $\mu\text{H/m}$	α	15.9 dB ^a	22 dB ^b
f_0	4.55 GHz	8.32 GHz	w	7.8 μm	8.0 μm
R_T	12.5 k Ω	10.0 k Ω	s	5.7 μm	6.1 μm
C_J	3 fF	3 fF			

^{a,b} The values experimentally measured with a control sample are 13.3 dB^a and 19.5 dB^b.

Supporting information:

Cryogenic microwave source based on nanoscale tunnel junctions

Shumpei Masuda, Kuan Y. Tan, Matti Partanen, Russell E. Lake, Joonas Govenius, Matti Silveri,
Hermann Grabert and Mikko Möttönen

Parameters

The fundamental resonance frequency of a homogeneous half-wavelength CPW resonator of length L_{res} is given by

$$f_0 = \frac{c}{2L_{\text{res}}\sqrt{\epsilon_{\text{eff}}}} \quad (\text{S1})$$

where the speed of light in vacuum is denoted by c and the effective relative permittivity of the resonator by ϵ_{eff} . The CPW capacitance c_{res} and inductance l_{res} per unit length can be expressed as^{37,38}

$$\begin{aligned} c_{\text{res}} &= 4\epsilon_0\epsilon_{\text{eff}}\frac{K(k_0)}{K(k'_0)}, \\ l_{\text{res}} &= \frac{\mu_0 K(k'_0)}{4K(k_0)}, \end{aligned} \quad (\text{S2})$$

where K is the complete elliptic integral of the first kind and

$$\begin{aligned} k_0 &= \frac{w}{w+2s}, \\ k'_0 &= \sqrt{1-k_0^2}, \end{aligned} \quad (\text{S3})$$

depend on the width of the center conductor w , and on the separation between the center conductor and the ground plane of the CPW resonator s . We calculate c_{res} and l_{res} in Eq. (S2) using Eqs. (S1)

and (S3) and the measured values for f_0 , L_{res} , w , and s given in Table 1. We neglect the kinetic inductance because it is sufficiently smaller than the geometric inductance in Eq. (S2),³⁸ although in principle, the total inductance per unit length is the sum of the geometric and the kinetic contributions. The resonance frequency calculated using Eq. (S1) and the analytic form of ϵ_{eff} for an unshielded CPW³⁷ has less than 1% difference from the measured value for Sample A and about 4% deviation for Sample B. The characteristic impedance Z_0 of the transmission line is obtained from $Z_0 = \sqrt{l_{\text{res}}/c_{\text{res}}}$.

Capacitances C_k for $k \in \{1, 2, 3, 4\}$ are estimated using

$$C_k = \frac{A_k \epsilon}{d}, \quad (\text{S4})$$

where A_k is the area of the parallel-plate capacitor, the permittivity of the aluminum oxide dielectric is denoted by $\epsilon \approx 9.8 \times \epsilon_0$, where ϵ_0 is the permittivity of vacuum, and $d = 50$ nm is the thickness of the aluminum oxide layer. The capacitance density used for C_J is 75 fF/ μm^2 . The tunnel junction area is approximately 200×200 nm² inferred from the SEM image of the sample.

In the absence of an electromagnetic environment, the current through an NIS junction is given by

$$I(V_B) = \frac{1}{eR_T} \int_{-\infty}^{\infty} dE \left[n_S(E) f(E, T_S) [1 - f(E + eV_B/2, T_N)] - n_S(E - eV_B/2) [1 - f(E - eV_B/2, T_S)] f(E, T_N) \right], \quad (\text{S5})$$

where T_N is the electron temperature of the normal-metal island obtained using the thermometer junctions. The superconductor density of states n_S is represented by

$$n_S(E) = \left| \text{Re} \left[\frac{E/\Delta + i\gamma_D}{\sqrt{(E/\Delta + i\gamma_D)^2 - 1}} \right] \right|, \quad (\text{S6})$$

where γ_D is the Dynes parameter¹⁵ and f is the Fermi–Dirac distribution function

$$f(E, T) = \frac{1}{e^{E/(k_B T)} + 1}. \quad (S7)$$

The tunnel resistance R_T , the Dynes parameter, and the superconductor gap parameter Δ are obtained from a fit of Eq. (S5) to measured junction IV characteristics.

Apparent transmission line temperature

In our thermal model in Figure 3, the resonator is thermally connected only to the transmission line and to the tunneling electrons. Due to the simple way the transmission line heats the resonator given by Eq. (1) however, any additional constant heating power to the resonator is accounted in this model by an adjustment of the average photon number of the transmission line. This gives rise to the apparent temperature of the transmission line, T_{TL} , connected to the average photon number, \bar{n}_{TL} , through the Bose distribution function. Note that \bar{n}_{TL} is independent of the bias voltage since also the electron temperature of the 50- Ω resistor in Figure 1d giving rise to the photons incident on the resonator does not change with the bias voltage.

Since the power arising from the photon-assisted tunneling is negligible at zero bias voltage, we have $P_{RT} = 0$ in Eq. (1), and hence $T_{res} = T_{TL}$ at zero bias. Thus if we find T_{TL} at any bias voltage, we obtain the temperature and the average photon number of the resonator at zero bias. Consequently, we obtain these quantities at any bias voltage using Eq. (1) and the directly measured power change between the finite and zero bias points.

We use the bias point, at which the measured power change crosses zero, as the calibration voltage for T_{TL} . Here, the net output power given by Eq. (1) and hence the temperature of the resonator coincides with that at zero bias. Thus the power arising from photon-assisted tunneling, P_{JR} , must vanish. As we show in the next section, this calibration point is independent of many of the sample parameters such as the tunnel resistance, R_T . It is also independent of the gain of our amplification chain. Thus our model accurately yields the resonator temperature at the calibration

point which equals the apparent transmission line temperature.

Energy transfer between tunneling electrons and the resonator

The electron tunneling may lead to creation and annihilation of photons at the resonator giving rise to the power transfer P_{JR} in Figure 3. To this end, we employ the $P(E)$ theory which has been developed to obtain the electron tunneling rates across tunnel junctions and the resulting energy transfer to the environment.²⁵ In terms of the $P(E)$ theory, the environment refers to the electrical degrees of freedom which are coupled to the tunneling process.

The power transfer to the environment strongly depends on the electrical impedance of the system. A simplified electrical circuit diagram of our system is depicted in Figure S1a. The first harmonic mode of the CPW resonator is modeled as a parallel LC circuit with capacitance $C_L = c_{\text{res}}L_{\text{res}}/2$, inductance $L_L = 2l_{\text{res}}L_{\text{res}}/\pi^2$ and angular frequency $\omega_0 = 1/\sqrt{C_LL_L}$. We assume that the electron tunneling event on either of the junctions is hardly affected by another junction because of a small junction capacitance C_J and large tunneling resistance R_T , and that the direct influence of the transmission line to the electron tunneling is neglected due to a relatively small coupling capacitance C_4 . Thus, we consider a pair of separate effective circuits depicted in Figures S1b,c to calculate the tunneling rate at each NIS junction. We assume that the resistance of the normal-metal island is small enough to be neglected because it is in series with the small junction capacitance, and hence negligible current flows through it with respect to Ohmic losses.

The power from the tunneling electrons to the environment is represented by

$$P_{\text{env}}(V_B/2, T_S, T_N) = 2[\vec{P}(V_B/2, T_S, T_N) + \overleftarrow{P}(V_B/2, T_S, T_N)], \quad (\text{S8})$$

where the powers caused by the forward and the backward electron tunneling events at each junc-

tion are given by²⁵

$$\begin{aligned}
\vec{P}(V_B/2, T_S, T_N) &= \frac{1}{e^2 R_T} \iint_{-\infty}^{\infty} dE dE' n_S(E) f(E, T_S) [1 - f(E' + eV_B/2, T_N)] \\
&\quad \times (E - E') P(E - E', T_{\text{env}}), \\
\overleftarrow{P}(V_B/2, T_S, T_N) &= \frac{1}{e^2 R_T} \iint_{-\infty}^{\infty} dE dE' n_S(E' - eV_B/2) [1 - f(E' - eV_B/2, T_S)] f(E, T_N) \\
&\quad \times (E - E') P(E - E', T_{\text{env}}),
\end{aligned} \tag{S9}$$

respectively. Here, T_S and T_{env} denote the temperatures of the superconductor and of the environment, respectively. The factor of two in Eq. (S8) arises from the fact that the two effective circuits in Figure S1b have an identical contribution to the power. The probability density $P(E)$ for the environment to absorb energy E during a tunneling event is expressed as²⁵

$$P(E, T_{\text{env}}) = \frac{1}{2\pi\hbar} \int_{-\infty}^{\infty} dt \exp[J(t, T_{\text{env}})] \exp\left[i\frac{E}{\hbar}t\right], \tag{S10}$$

where

$$J(t, T_{\text{env}}) = 2 \int_0^{\infty} \frac{d\omega}{\omega} \frac{\text{Re}[Z_t(\omega)]}{R_K} \left[\coth\left(\frac{\hbar\omega}{2k_B T_{\text{env}}}\right) [\cos(\omega t) - 1] - i \sin(\omega t) \right], \tag{S11}$$

and

$$\text{Re}[Z_t] = \frac{\pi}{2C_L} [\delta(\omega - \omega_0) + \delta(\omega + \omega_0)] + \frac{\pi}{2} \frac{C_{1(2)} + C_3}{C_{1(2)} C_3} \delta(\omega). \tag{S12}$$

In $P(E)$ theory, the effective impedance Z_t in Eq. (S11) is the impedance of the external circuit $Z_{1/2}$ in parallel with C_J . The influence of C_J , which is approximately 3 fF $\ll C_{1/2/3}$, to the effective impedance is neglected in Eq. (S12) because Z_t is dominated by $Z_{1/2}$. The influence of $C_{1/2}$ is also negligible because it is more than 50 times larger than C_3 and approximately cancel out in Eq. (S12).

Note that the environment consists not only of the resonator but also of the capacitors $C_{1/2/3}$.

Finite $C_{1/2/3}$ broadens the peaks of $P(E)$ which become delta functions in the limit of infinite $C_{1/2/3}$. Figure S2a shows $P(E)$ of Sample A for various T_{res} at $eV_{\text{B}}/(2\Delta) = 1.2$, where we assumed $T_{\text{env}} = T_{\text{res}}$. The peaks at $E = \hbar\omega_0 \approx 0.09 \times \Delta$ and $E = -\hbar\omega_0 \approx -0.09 \times \Delta$ correspond to the emission and absorption of a single photon from the resonator, respectively. The high peak at $E = 0$ corresponds to the elastic tunnelling. We assume that only the peaks at $|E| = \pm\hbar\omega_0$ contribute to P_{JR} . Thus, only a part of P_{env} contributes to P_{JR} . We compute P_{JR} using Eqs. (S8) and (S9) where we first replace P by

$$\begin{aligned} P_{\text{M}}(E, T_{\text{res}}) &= P(E, T_{\text{res}}) \text{ for } |E| \geq \hbar\omega_0/2, \\ &= 0 \quad \text{for } |E| < \hbar\omega_0/2. \end{aligned} \quad (\text{S13})$$

As shown in Figure S2a, the peaks become broader with increasing T_{res} . The center peak and the side peaks are not well separated for high T_{res} . Thus, the numerical results of Sample A may have considerable error beyond $eV/(2\Delta) = 1.4$ corresponding to $T_{\text{res}} > 500$ mK [see Figure 2d]. The minor discrepancy between the numerical and experimental results in Figure 2c is attributed to this fact. Figure S2b shows the dependence of $P(E)$ on the coupling capacitance C_3 . The peak becomes narrower for larger C_3 due to the increasing coupling strength between a tunneling electron and the resonator.

Energy transfer between the resonator and the transmission line

Let us study a model for the energy transfer between a CPW resonator and a transmission line which are mutually capacitively coupled as shown in Figure S3. First, we model the transmission line as a CPW resonator of finite length and finally extend the length to infinity. The electrostatic energy of the coupling capacitor C_4 is given by the voltage difference between the resonator and the transmission line as $C_4(V_{\text{TL}} - V_{\text{res}})^2/2$, where V_{res} and V_{TL} are the voltage of the resonator and the transmission line at the capacitor, respectively. Thus, the interaction Hamiltonian between the

resonator and the transmission line is represented as

$$\hat{H}_{\text{int}} = -C_4 \hat{V}_{\text{res}} \hat{V}_{\text{TL}}. \quad (\text{S14})$$

The voltage operators of the resonator \hat{V}_{res} and of the transmission line \hat{V}_{TL} are represented as $\hat{V}_{\text{res}} = \sum_M V_M^{(\text{res})} (\hat{a}_M^\dagger + \hat{a}_M)$ and $\hat{V}_{\text{TL}} = \sum_N V_N^{(\text{TL})} (\hat{b}_N^\dagger + \hat{b}_N)$, respectively, with the creation operator \hat{a}_M^\dagger and the annihilation operator \hat{a}_M of a photon in the M th mode of the resonator and the creation operator \hat{b}_N^\dagger and the annihilation operator \hat{b}_N of a photon in the N th mode of the transmission line.² The coefficients are written as $V_M^{(\text{res})} = \sqrt{M\hbar\omega_{\text{res}}/(L_{\text{res}}c_{\text{res}})}$ and $V_N^{(\text{TL})} = \sqrt{N\hbar\omega_{\text{TL}}/(L_{\text{TL}}c_{\text{TL}})}$ with the fundamental resonance frequencies $\omega_{\text{res/TL}} = \pi/(L_{\text{res/TL}}\sqrt{l_{\text{res/TL}}c_{\text{res/TL}}})$. The length of the resonator (transmission line) is L_{res} (L_{TL}), the capacitance per unit length is c_{res} (c_{TL}) and the inductance per unit length is l_{res} (l_{TL}). Above, we have assumed that C_4 is so small that its effect on $\omega_{\text{res/TL}}$ and the operators may be neglected.

We employ a basis composed of the energy eigenstates of an uncoupled resonator–transmission-line system. Assuming weak coupling, we may estimate the transition rate from an energy eigenstate $|i\rangle = |m_1, m_2, \dots; n_1, n_2, \dots\rangle$ to a different one $|f\rangle = |m'_1, m'_2, \dots; n'_1, n'_2, \dots\rangle$ using Fermi's golden rule, where m_M (n_N) denotes the number of photons in the M th (N th) mode of the resonator (transmission line). The Hamiltonian in Eq. (S14) is rewritten as

$$\hat{H}_{\text{int}}^{\text{eff}} = -C_4 \sum_M \sum_N V_M^{(\text{res})} V_N^{(\text{TL})} (\hat{a}_M^\dagger \hat{b}_N + \hat{a}_M \hat{b}_N^\dagger), \quad (\text{S15})$$

where we omitted the terms proportional to $\hat{a}_M^\dagger \hat{b}_N^\dagger$ and $\hat{a}_M \hat{b}_N$ which do not contribute to the transition rates in Fermi's golden rule. We first consider the case where a photon in the I th mode of the resonator is annihilated and a photon in the J th mode of the transmission line is created, i.e., we only consider the term $-C_4 V_I^{(\text{res})} V_J^{(\text{TL})} \hat{a}_I \hat{b}_J^\dagger$ in Eq. (S15). Consequently, the probability $P_{if}(t)$ that

we find the state $|f\rangle$ at time t starting from $|i\rangle$ is given by Fermi's golden rule as

$$P_{if}^{(IJ)}(t) = t \frac{2\pi}{\hbar} C_4^2 (V_I^{(\text{res})})^2 (V_J^{(\text{TL})})^2 m_I (n_J + 1) \times \delta(E_f - E_i) \delta_{m'_I, m_I - 1} \delta_{n'_J, n_J + 1} \left(\prod_{K \neq I} \delta_{m'_K, m_K} \right) \left(\prod_{K \neq J} \delta_{n'_K, n_K} \right), \quad (\text{S16})$$

where $E_f - E_i = \hbar(\omega_{\text{TL}}^{(J)} - \omega_{\text{res}}^{(I)})$ with $\omega_{\text{TL}}^{(J)} = J\omega_{\text{TL}}$ and $\omega_{\text{res}}^{(I)} = I\omega_{\text{res}}$.

Let us calculate the probability $P_i^{(+)}(t)$ that a photon in the I th mode of the resonator is annihilated and a photon in the transmission line is created. To this end, we sum up the probabilities for all photon numbers and every mode J in the transmission line. First, we execute the summation over the final photon numbers, which results in

$$P_i^{(IJ)} = t \frac{2\pi}{\hbar} C_4^2 (V_I^{(\text{res})})^2 (V_J^{(\text{TL})})^2 m_I (n_J + 1) \delta[\hbar(\omega_{\text{TL}}^{(J)} - \omega_{\text{res}}^{(I)})]. \quad (\text{S17})$$

Next we sum with respect to J in the limit where L_{TL} extends to infinity. Thus, we replace the discrete summation over J by an integral with respect to energy using the relation

$$\lim_{L_{\text{TL}} \rightarrow \infty} \frac{1}{\Delta E_J} \sum_J \Delta E_J = \lim_{L_{\text{TL}} \rightarrow \infty} \frac{1}{\Delta E_J} \int_0^\infty dE_J, \quad (\text{S18})$$

where $\Delta E_J = \hbar\omega_{\text{TL}} = \hbar\pi/(L_{\text{TL}}\sqrt{l_{\text{TL}}c_{\text{TL}}})$. Using Eq. (S18) to sum over J in Eq. (S17), the probability of a photon in the I th mode to decay given the initial state $|i\rangle$ is represented by

$$\begin{aligned} P_i^{(I)}(t) &= \lim_{L_{\text{TL}} \rightarrow \infty} \sum_J P_i^{(IJ)}(t) \\ &= \frac{2L_{\text{TL}}\sqrt{l_{\text{TL}}c_{\text{TL}}}}{\hbar^2} C_4^2 (V_I^{(\text{res})})^2 (V_J^{(\text{TL})})^2 m_\omega (n_\omega + 1)t \\ &= 2C_4^2 \frac{\omega^2 Z_0}{L_{\text{res}}c_{\text{res}}} m_\omega (n_\omega + 1)t \end{aligned} \quad (\text{S19})$$

where $Z_0 = \sqrt{l_{\text{TL}}/c_{\text{TL}}}$ and we have introduced a notation $m_\omega := m_I$ and n_ω is the photon number in the initial state of the transmission line corresponding to the mode with angular frequency $\omega :=$

$\omega_{\text{res}}^{(I)}$.

Considering all the possible initial states with different photon numbers, the probability of annihilating a photon in the resonator mode I , $P_I^{(+)}$, may be represented as

$$\begin{aligned} P_{\omega}^{(+)}(t) &:= P_I^{(+)}(t) = \sum_{m_{\omega}} \sum_{n_{\omega}} p_{m_{\omega}} p_{n_{\omega}} P_i^{(I)}(t) \\ &= 2C_4^2 \frac{\omega^2 Z_0}{L_{\text{res}} c_{\text{res}}} \bar{m}_{\omega} (\bar{n}_{\omega} + 1) t, \end{aligned} \quad (\text{S20})$$

where the average photon numbers with angular frequency ω in the resonator and the transmission line are denoted by \bar{m}_{ω} and \bar{n}_{ω} , respectively. Here, $p_{m_{\omega}}$ ($p_{n_{\omega}}$) is the probability that there are m_{ω} (n_{ω}) photons with angular frequency ω in the resonator (transmission line) in the initial state. Hereafter, we replace $P_I^{(+)}$ by $P_{\omega}^{(+)}$ for simplicity of notation. Thus, the rate that photons in the resonator with the energy $\hbar\omega$ transfer to the transmission line is obtained as

$$\Gamma_{\text{res,TL}}^{(\omega)} = \frac{dP_{\omega}^{(+)}}{dt} = 2C_4^2 \frac{\omega^2 Z_0}{L_{\text{res}} c_{\text{res}}} \bar{m}_{\omega} (\bar{n}_{\omega} + 1). \quad (\text{S21})$$

In the same manner the photon transition rate from the transmission line to the resonator is obtained as

$$\Gamma_{\text{TL,res}}^{(\omega)} = 2C_4^2 \frac{\omega^2 Z_0}{L_{\text{res}} c_{\text{res}}} (\bar{m}_{\omega} + 1) \bar{n}_{\omega}. \quad (\text{S22})$$

The total power from the resonator to the transmission line mediated by the photons with angular frequency ω is represented with the photon numbers in the resonator and the transmission line as

$$\begin{aligned} P_{\text{RT}}^{(\omega)} = \hbar\omega [\Gamma_{\text{res,TL}} - \Gamma_{\text{TL,res}}] &= 2C_4^2 \frac{\hbar\omega^3 Z_0}{L_{\text{res}} c_{\text{res}}} (\bar{m}_{\omega} - \bar{n}_{\omega}) \\ &= C_4^2 \frac{\hbar\omega^3 Z_0}{C_L} (\bar{m}_{\omega} - \bar{n}_{\omega}). \end{aligned} \quad (\text{S23})$$

In the thermal state, we have

$$\begin{aligned}\bar{m}_\omega &= \frac{1}{e^{\hbar\omega/(k_B T_{\text{res}})} - 1}, \\ \bar{n}_\omega &= \frac{1}{e^{\hbar\omega/(k_B T_{\text{TL}})} - 1},\end{aligned}\tag{S24}$$

and hence

$$P_{\text{RT}}^{(\omega)} = C_4^2 \frac{\hbar\omega^3 Z_0}{C_L} \left[\frac{1}{e^{\hbar\omega/(k_B T_{\text{res}})} - 1} - \frac{1}{e^{\hbar\omega/(k_B T_{\text{TL}})} - 1} \right],\tag{S25}$$

owing to Eq. (S23).

Thermometry

A pair of current-biased NIS junctions is used as a thermometer as illustrated in Figure 1b. The voltage V_{th} across the thermometer junctions provides a good measure of the electron temperature T_{N} of the normal-metal island in the temperature range of interest to us. In $P(E)$ theory, the tunnel current is written as²⁵

$$\begin{aligned}I_{\text{th}}(V_{\text{th}}, T_{\text{N}}, T_{\text{S}}, T_{\text{env}}) &= \frac{1}{eR_{\text{T}}} \iint_{-\infty}^{\infty} dE dE' \left[n_{\text{S}}(E) f(E, T_{\text{S}}) [1 - f(E' + eV_{\text{th}}/2, T_{\text{N}})] \right. \\ &\quad \left. - n_{\text{S}}(E' - eV_{\text{th}}/2) [1 - f(E' - eV_{\text{th}}/2, T_{\text{S}})] f(E, T_{\text{N}}) \right] P(E - E', T_{\text{env}}).\end{aligned}\tag{S26}$$

The current in Eq. (S26) is approximated by

$$\begin{aligned}I_{\text{th}}(V_{\text{th}}, T_{\text{N}}) &= \frac{1}{eR_{\text{T}}} \int_{-\infty}^{\infty} dE \left[n_{\text{S}}(E) f(E, T_{\text{S}}) [1 - f(E + eV_{\text{th}}/2, T_{\text{N}})] \right. \\ &\quad \left. - n_{\text{S}}(E - eV_{\text{th}}/2) [1 - f(E - eV_{\text{th}}/2, T_{\text{S}})] f(E, T_{\text{N}}) \right],\end{aligned}\tag{S27}$$

where we replaced $P(E - E', T_{\text{env}})$ by $\delta(E - E')$ because in our case, the current is dominated by the elastic electron tunneling. Here, we neglect the dependence of I_{th} on T_{S} justified by $k_B T_{\text{S}} \ll \Delta$.

Thus, the voltage V_{th} essentially depends only on I_{th} and T_{N} . For a fixed value of I_{th} , V_{th} can be regarded as a single-valued function of T_{N} . We utilize this property to convert the measured V_{th} into T_{N} .

Figure S4a shows the thermometer voltage as a function of the bath temperature T_0 measured for $I_{\text{th}} = 17.7$ pA and vanishing bias voltage at the other junctions, $V_{\text{B}} = 0$. The experimental value of $V_{\text{th}}(T_0)$ matches the theoretical value obtained from Eq. (S27) for $V_{\text{th}}(T_{\text{N}} = T_0)$ and $T_0 \gtrsim 100$ mK. This is because the electron temperature of the normal-metal island is close to the bath temperature for high T_0 . The agreement of the theoretical and numerical results shows that this model of the thermometer is accurate. On the other hand, the experimental values of V_{th} are lower than the theoretical ones at $T_0 < 100$ mK since the electrons thermally decouple from the phonons leading to a saturation of the electron temperature.¹⁵ Nevertheless, the theoretical model can be used to convert the measured V_{th} to T_{N} even in this temperature range and under finite V_{B} . Figure S4b shows the measured T_{N} for several bias voltages obtained using the calibration data in Figure S4a.

References

- (1) Wolf, E. L. *Quantum Nanoelectronics: An Introduction to Electronic Nanotechnology and Quantum Computing* (Wiley-VCH, Weinheim, 2009).
- (2) Blais, A., Huang, R. -S., Wallraff, A., Girvin, S. M. & Schoelkopf, R. J. Cavity quantum electrodynamics for superconducting electrical circuits: An architecture for quantum computation. *Phys. Rev. A* **69**, 062320 (2004).
- (3) Wallraff, A., Schuster, D. I., Blais, A., Frunzio, L., Huang, R.-S., Majer, J., Kumar, S., Girvin, S. M. & Schoelkopf, R. J. Strong coupling of a single photon to a superconducting qubit using circuit quantum electrodynamics. *Nature* **431**, 162–167 (2004).
- (4) Majer, J., Chow, J. M., Gambetta, J. M., Koch, J., Johnson, B. R., Schreier, J. A., Frunzio, L., Schuster, D. I., Houck, A. A., Wallraff, A., Blais, A., Devoret, M. H., Girvin, S. M. & Schoelkopf, R. J. Coupling superconducting qubits via a cavity bus. *Nature* **449**, 443–447 (2007).
- (5) Sillanpää, M. A., Park, J. I. & Simmonds, R. W. Coherent quantum state storage and transfer between two phase qubits via a resonant cavity. *Nature* **449**, 438–442 (2007).
- (6) Devoret, M. H. & Schoelkopf, R. J. Superconducting circuits for quantum information: an outlook. *Science* **339**, 1169–1174 (2013).
- (7) Kelly, J. et al. State preservation by repetitive error detection in a superconducting quantum circuit. *Nature* **519**, 66–69 (2015).
- (8) Ofek, N. et al. Extending the lifetime of a quantum bit with error correction in superconducting circuits. *Nature* **536**, 441–445 (2016).
- (9) Inomata, K., Lin, Z. R., Koshino, K., Oliver, W. D., Tsai, J. S., Yamamoto, T. & Nakamura, Y. Single microwave-photon detector using an artificial Λ -type three-level system. *Nat. Commun.* **7**, 12303 (2016).

- (10) Govenius, J., Lake, R. E., Tan, K. Y. & Möttönen, M. Detection of Zeptojoule microwave pulses using electrothermal feedback in proximity-induced Josephson junctions. *Phys. Rev. Lett.* **117**, 030802 (2016).
- (11) Saira, O.-P., Zgirski, M., Viisanen, K. L., Golubev, D. S. & Pekola, J. P. Dispersive thermometry with a Josephson junction coupled to a resonator. *Phys. Rev. Applied* **6**, 024005 (2016).
- (12) Clark, A. M., Miller, N. A., Williams, S., Ruggiero, S. T., Hilton, G. C., Vale, L. R., Beall, K. D., Irwin, K. D. & Ullom, J. N. Cooling of bulk material by electron-tunneling refrigerators. *Appl. Phys. Lett.* **86**, 173508–173510 (2005).
- (13) Timofeev, A. V., Helle, M., Meschke, M., Möttönen, M. & Pekola, J. P. Electronic refrigeration at the quantum limit. *Phys. Rev. Lett.* **102**, 200801 (2009).
- (14) Tan, K. Y., Partanen, M., Lake, R. E., Govenius, J., Masuda, S. & Möttönen, M. Quantum-circuit refrigerator. *arXiv:1606.04728* (2016).
- (15) Giazotto, F., Heikkilä, T. T., Luukanen, A., Savin, A. M. & Pekola, J. P. Opportunities for mesoscopics in thermometry and refrigeration: Physics and applications. *Rev. Mod. Phys.* **78**, 217–274 (2006).
- (16) Hofheinz, M., Wang, H., Ansmann, M., Bialczak, R. C., Lucero, E., Neeley, M., O’Connell, A. D., Sank, D., Wenner, J., Martinis, J. M. & Cleland, A. N. Synthesizing arbitrary quantum states in a superconducting resonator. *Nature* **459**, 546–549 (2009).
- (17) Meschke, M., Guichard, W. & Pekola, J. P. Single-mode heat conduction by photons. *Nature* **444**, 187–190 (2006).
- (18) Partanen, M., Tan, K. Y., Govenius, J., Lake, R. E., Mäkelä, K., Tanttu, T. & Möttönen, M. Quantum-limited heat conduction over macroscopic distances. *Nat. Phys.* **12**, 460–464 (2016).

- (19) Houck, A. A., Schuster, D. I., Gambetta, J. M., Schreier, J. A., Johnson, B. R., Chow, J. M., Frunzio, L., Majer, J., Devoret, M. H., Girvin, S. M. & Schoelkopf, R. J. Generating single microwave photons in a circuit. *Nature* **449**, 328–331 (2007).
- (20) Peng, Z. H., de Graaf, S. E., Tsai, J. S. & Astafiev, O. V. Tuneable on-demand single-photon source in the microwave range. *Nat. Commun.* **449**, 12588 (2016).
- (21) Pekola, J. P., Maisi, V. F., Kafanov, S., Chekurov, N., Kemppinen, A., Pashkin, Y. A., Saira, O. -P., Möttönen M. & Tsai, J. S. Environment-assisted tunneling as an origin of the Dynes density of states. *Phys. Rev. Lett.* **105**, 026803 (2010).
- (22) Devoret, M. H., Esteve, D., Grabert, H., Ingold, G.-L. m Pothier, H. & Urbina, C. Effect of the electromagnetic environment on the Coulomb blockade in ultrasmall tunnel junctions. *Phys. Rev. Lett.* **64**, 1824 (1990).
- (23) Girvin, S. M., Glazman, L. I., Jonson, M., Penn, D. R. & Stiles, M. D. Quantum fluctuations and the single-junction Coulomb blockade. *Phys. Rev. Lett.* **64**, 3183 (1990).
- (24) Averin, B., Nazarov, Y. & Odintsov, A. Incoherent tunneling of the cooper pairs and magnetic flux quanta in ultrasmall Josephson junctions. *Physica B* **165/166**, 945–946 (1990).
- (25) Ingold, G. & Nazarov, Y. V. Charge tunneling rates in ultrasmall junctions. *NATO ASI Series B* **294**, 21–107 (1992).
- (26) Zakka-Bajjani, E., Dufouleur, J., Coulombel, N., Roche, P., Glattli, D. C. & Portier, F. Experimental determination of the statistics of photons emitted by a tunnel junction. *Phys. Rev. Lett.* **104**, 206802 (2010).
- (27) Hofheinz, M., Portier, F., Baudouin, Q., Joyez, P., Vion, D., Bertet, P., Roche, P. & Esteve, D. Bright side of the coulomb blockade. *Phys. Rev. Lett.* **106**, 217005 (2011).
- (28) You, J. Q., Liu, Y. X., Sun, C. P. & Nori, F. Persistent single-photon production by tunable on-chip micromaser with a superconducting quantum circuit. *Phys. Rev. B* **75**, 104516 (2007).

- (29) Astafiev, O., Inomata, K., Niskanen, A. O., Yamamoto, T., Pashkin, Y. A., Nakamura, Y. & Tsai, J. S. Single artificial-atom lasing. *Nature* **449**, 588–590 (2007).
- (30) Hauss, J., Fedorov, A., Hutter, C., Shnirman, A. & Schön, G. Single-qubit lasing and cooling at the Rabi frequency. *Phys. Rev. Lett.* **100**, 037003 (2008).
- (31) Grajcar, M., van der Ploeg, S. H. W., Izmalkov, A., Ilichev, H. G. M. E., Fedorov, A., Shnirman, A. & Schön, G. Sisyphus cooling and amplification by a superconducting qubit. *Nat. Phys.* **4**, 612–616 (2008).
- (32) Bruhat, L. E., Viennot, J. J., Dartiailh, M. C., Desjardins, M. M., Kontos, T. & Cottet, A. Cavity photons as a probe for charge relaxation resistance and photon emission in a quantum dot coupled to normal and superconducting continua. *Phys. Rev. X* **6**, 021014 (2016).
- (33) Stockklauser, A., Maisi, V. F., Basset, J., Cujia, K., Reichl, C., Wegscheider, W., Ihn, T., Wallraff, A. & Ensslin, K. Microwave emission from hybridized states in a semiconductor charge qubit. *Phys. Rev. Lett.* **115**, 046802 (2015).
- (34) Childress, L., Sørensen, A. S. & Lukin, M. D. Mesoscopic cavity quantum electrodynamics with quantum dots. *Phys. Rev. A* **69**, 042302 (2004).
- (35) Liu, Y.-Y., Petersson, K. D., Stehlik, J., Taylor, J. M. & Petta, J. R. Photon emission from a cavity-coupled double quantum dot. *Phys. Rev. Lett.* **113**, 036801 (2014).
- (36) Leivo, M. M. & Pekola, J. P. *Appl. Phys. Lett.* **68**, 1996–1998 (1996).
- (37) Gevorgian, S., Linnér, L. J. P. & Kollberg, E. L. CAD models for shielded multilayered CPW. *IEEE Trans. Microw. Theory Techn.* **43**, 772–779 (1995).
- (38) Göppl, M., Fragner, A., Baur, M., Bianchetti, R., Filipp, S., Fink, J. M., Leek, P. J., Puebla, G., Steffen, L. & Wallraff, A. Coplanar waveguide resonators for circuit quantum electrodynamics. *J. Appl. Phys.* **104**, 113904–113911 (2008).

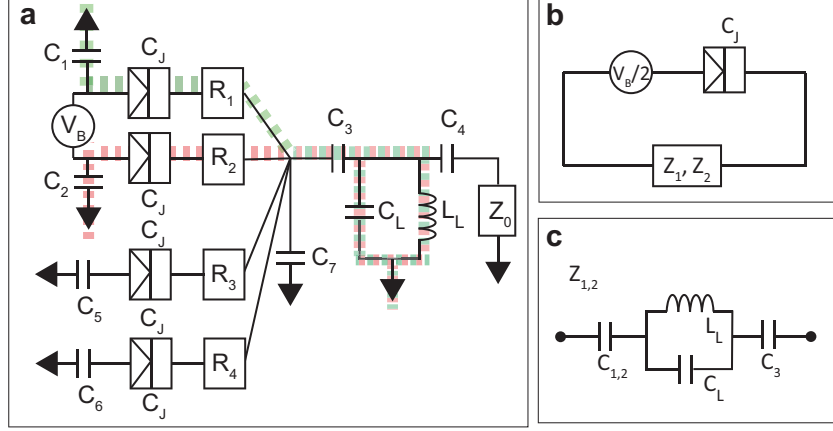


Figure S1: (a) Circuit model of the realized microwave source. The resonator is modelled by a single parallel LC circuit. See Figure 1 for the definition of the capacitances. The resistances arise from the finite conductance of the normal-metal island of the NIS junctions. (b) Effective circuits for photon-assisted tunneling at each NIS junction. The systems with Z_1 and Z_2 correspond to the red and green conduction paths in panel (a), respectively. (c) Composition of the impedance elements Z_1 and Z_2 . Here, the finite conductance of the normal-metal island and the direct interplay between the electron tunneling and losses to the transmission line described by Z_0 have been neglected.

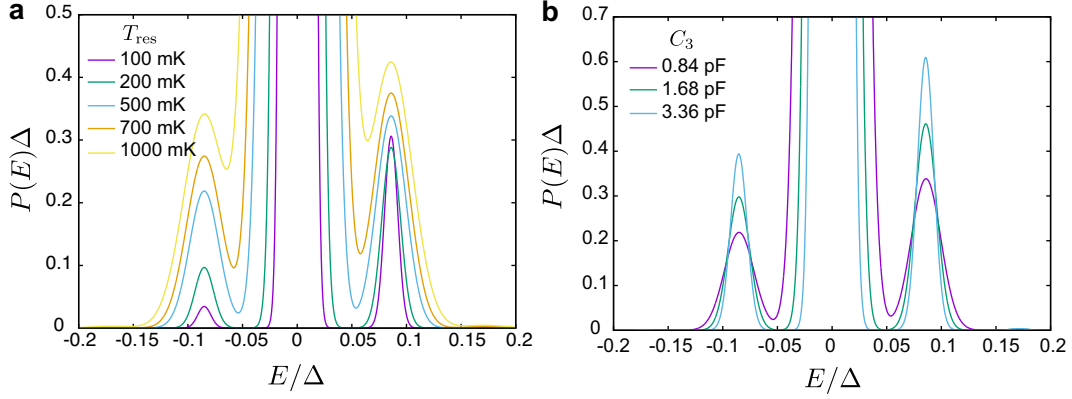


Figure S2: (a) $P(E)$ function of Sample A for $eV_B/(2\Delta) = 1.2$ and T_{res} as indicated. The other parameters are given in Table 1. (b) $P(E)$ of Sample A shown for various indicated C_3 , for $T_{\text{res}} = 500$ mK and $eV/(2\Delta) = 1.2$.

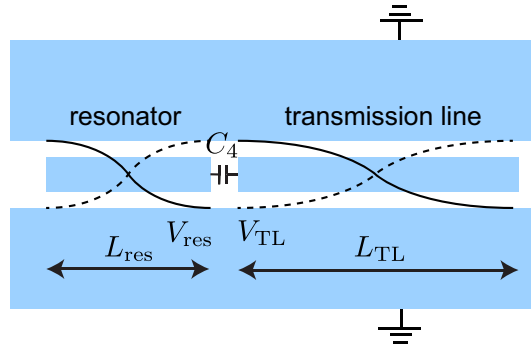


Figure S3: Illustration of a CPW resonator and a transmission line coupled by capacitance C_4 . The solid and the dashed lines represent the voltage difference between the center conductor and the ground plane. The transmission line is modelled by a CPW resonator with length L_{TL} which is eventually extended to infinity.

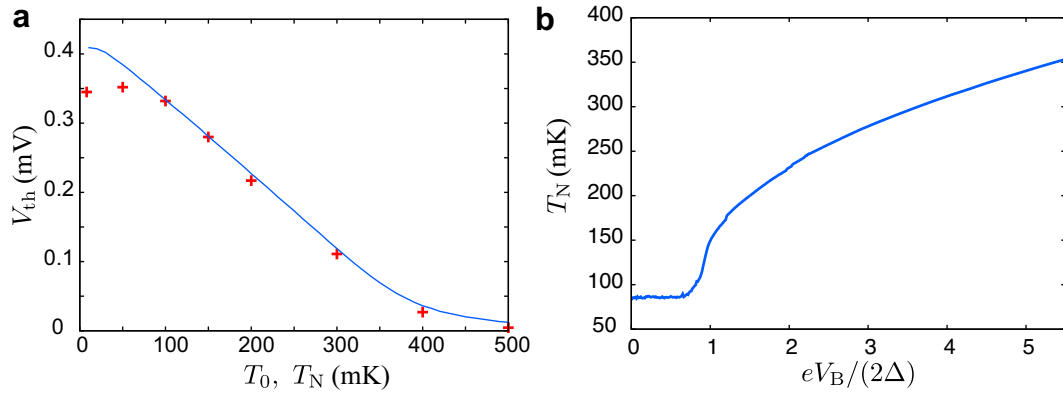


Figure S4: (a) Measured voltage (markers) V_{th} across the two thermometer junctions of Sample A as a function of the phonon bath temperature T_0 for $V_B = 0$ and $I_{th} = 17.7$ pA. The solid line shows V_{th} as a function of the electron temperature T_N as calculated using Eq. (S27). This result serves as the conversion function from V_{th} into T_N . (b) Measured electron temperature as a function of the bias voltage V_B in the case of Figure 2c,d.